Lab on a Chip

PAPER

View Article Online
View Journal | View Issue

Cite this: *Lab Chip*, 2026, **26**, 591

In situ imaging of fluid dynamics and nanocarrier nucleation inside microfluidic mixing devices

Christopher Hauss,[a] Alexander Erb,[b] Johannes Most,[a] Johanna Steinmann,[b] Robert W. Stark,[b] Stefanie Gier[a] and Maike Windbergs[*a]

Although microfluidic-based nanoprecipitation represents a powerful approach for the reproducible fabrication of various nanosized drug carrier systems, industrial translation remains limited. While versatile chip designs implementing advanced mixing elements exist, analytical tools for elucidating the precipitation mechanism, identifying critical process parameters, and monitoring carrier formation within the chip are sparse. Conventional characterization methods used for micromixers, such as tracing fluorescent dyes and/or computational fluid dynamics simulations, provide mostly indirect, often only two-dimensional insight, limiting their predictive value for scale-up and regulatory translation. In this study, a novel toolset combining confocal Raman and confocal fluorescence microscopy, as well as Foerster resonance energy transfer microscopy, was established to monitor solvent fluid dynamics and the *in situ* self-assembly of liposomes under varying flow conditions within a serpentine micromixer. This integrative approach enabled real-time spatial resolution of nanocarrier formation within the microfluidic device, confirming that vesicle formation predominantly occurs at the interface between the aqueous and ethanolic phases, underscoring the robustness of the setup. Beyond advancing mechanistic insight, the complementary use of two confocal microscopy techniques and a Foerster resonance energy transfer-based method offers a powerful toolset for process optimization and in-process quality control. Coupled with advances in additive manufacturing, this approach paves the way for rational micromixer design and the scalable production of microfluidic nanocarrier-based therapeutics, overcoming limitations and accelerating the industrial large-scale production of nanosized therapeutics.

Received 6th October 2025,
Accepted 7th January 2026

DOI: 10.1039/d5lc00947b

rsc.li/loc

Introduction

Nanoscale delivery systems are emerging as versatile and customizable drug carriers, enabling increasingly more sophisticated therapeutic strategies. Despite extensive research efforts, however, only a limited number of nanoparticulate systems have gained regulatory approval. This persistent gap in bench-to-bedside translation can largely be attributed to challenges in process scalability and reproducibility, both critical determinants of successful regulatory approval. Depending on the materials used and the intended application, nanocarriers can be fabricated using either top-down or bottom-up bulk fabrication approaches. While the former are based on size reduction processes that convert larger materials into nanoparticulate structures (*e.g.*, milling), the latter comprise methods that depend on the self-assembly of nano-sized building blocks.[1–3] However, such conventional fabrication methods often face batch-to-batch variability and offer limited control over the final formulation parameters.[4,5] Particle size and uniformity are crucial for the actual *in vivo* performance and delivery efficacy of the carrier systems, and regulatory agencies, such as the FDA, currently define size distribution as a critical quality attribute in formulation development.[6,7] Moreover, conventional bulk fabrication processes often expose formulations to high shear stress or fluctuating pH and temperature settings, making them unsuitable for labile biomolecules such as nucleic acids and proteins.[8,9] These limitations have fueled increasing interest in alternative strategies that provide milder conditions and improved process control, particularly for sensitive biological payloads. One promising approach is continuous nanoprecipitation, which allows the spontaneous formation of nanocarriers through the rapid mixing of an ethanolic lipid phase with an aqueous buffer.[10] A notable milestone in the application of this technology was the development of lipid nanocarrier (LNP) formulations for mRNA vaccines during the COVID-19 pandemic. The rapid, scalable fabrication of LNPs

[a] *Institute of Pharmaceutical Technology, Goethe University Frankfurt, Max-von-Laue-Str. 9, 60438 Frankfurt am Main, Germany. E-mail: windbergs@em.uni-frankfurt.de*
[b] *Physics of Surfaces, Technical University Darmstadt, Peter-Grünberg-Str. 16, 64206 Darmstadt, Germany*

using continuous nanoprecipitation techniques, such as the impingement jet mixer, underscores the potential of these methods for clinical translation.[11–13]

Building on the principles of nanoprecipitation, microfluidic mixing technologies have emerged as a next-generation platform for nanocarrier fabrication. Operating on the same fundamental mixing principle, these technologies enable the controlled and continuous fabrication of nanocarriers with customizable properties and improved reproducibility.[7,14] In particular, microfluidic mixers allow precise control over nanocarrier size and distribution by adjusting parameters such as total flow rate (TFR) and flow rate ratio (FRR), making them highly attractive for applications that demand consistent, customizable nanocarriers. While microfluidic-based approaches address many of the limitations of bulk methods, their optimization for high-throughput and industrial applications remains a significant challenge. Scaling up microfluidic systems for industrial standards requires increased TFRs, which in turn demand device geometries that maintain product quality across changing flow regimes.[4,14] Quality and performance are often evaluated under different flow conditions by analyzing nanocarriers of identical composition, produced at varying TFRs. The focus remains mainly on the hydrodynamic diameter and polydispersity index (PDI), which can be measured *via* dynamic light scattering (DLS). Internal flow profiles are either predicted *in silico* using computational fluid dynamics (CFD) or experimentally approximated by labeling the ethanolic phase with a fluorescent dye and visualizing its distribution *via* fluorescence microscopy.[15–17] CFD simulations and fluorescence-based imaging techniques typically offer only two-dimensional insight into inherently three-dimensional systems and remain primarily indirect. It is also unclear whether fluorescent dyes can accurately reflect the ethanol distribution within the channels and whether the added markers influence fluid–fluid interactions.[18] Critically, most current approaches do not permit direct, real-time visualization of nanocarrier nucleation or growth. Although the physicochemical mechanisms underlying particle assembly *via* nanoprecipitation are well established, the spatial resolution and flow-pattern dependence within microfluidic mixers remain poorly characterized. Yet, gaining deeper insight is essential for the rational design of microfluidic mixers and the accelerated development of scalable, robust manufacturing platforms.

To bridge this gap, this study introduces a novel approach that combines three complementary analytical techniques to directly visualize and evaluate flow behavior, fluid-phase mixing, and *in situ* nanocarrier formation in a chip. Using a serpentine micromixer with rectangular baffles to generate liposomes in a water/ethanol system, internal flow patterns were characterized computationally using CFD and experimentally using confocal fluorescence microscopy (CFM) with rhodamine B as a tracer. Ethanol distribution was further assessed *via* label-free confocal Raman microscopy (CRM). Crucially, nanocarrier formation was tracked *in situ via* Foerster resonance energy transfer (FRET) microscopy and further evaluated using characteristic Raman peaks.

Materials and methods

Micromixer design

A microfluidic serpentine channel with 20 alternating rectangular baffles adapted from Kimura *et al.* was used, as shown in Fig. 1.[19] The 150 μm-wide (w_b) baffles reduced the width of the main channel from 200 μm (w_c) to 50 μm (n). The spacing of the baffles (i), as well as their length (b), was set to 100 μm, resulting in a subsequent widening of the channel. The height of the entire microfluidic chip was set to 100 μm (h).

3D printing of molds for soft lithography

The geometry was designed using Autodesk Fusion (Autodesk Inc., San Rafael, CA, USA) and sliced with Voxeldance Additive (Voxeldance Inc., Shanghai, China). Molds were subsequently fabricated with a microArch S240A printer (Boston Microfabrication, Shenzhen, China) using a commercially available photo resin (HTL20, Boston Microfabrication, Shenzhen, China). Printed parts were cleaned with isopropanol and post-cured using a Form Cure device (Formlabs Inc., Somerville, MA, USA). Surface functionalization of the molds was performed by chemical vapor deposition of dimethyl chlorosilane (Sigma-Aldrich Co., St. Louis, MO, USA) in a desiccator at 250 mbar for at least 30 min.

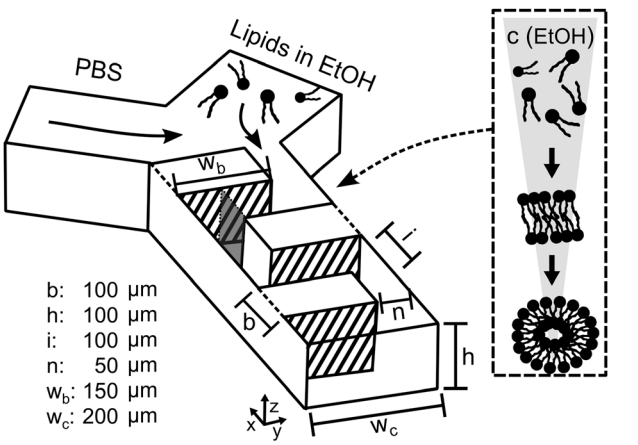

Fig. 1 Schematic illustration of the microfluidic device geometry and operating principle. The PDMS-based serpentine micromixer was adapted from Kimura *et al.* and featured one central channel with a width of 200 μm (w_c) and a height of 100 μm (h).[19] The channel is constricted by evenly spaced rectangular baffles with a width of 150 μm (w_b), narrowing it to 50 μm (n). In total, the mixing structure consists of 20 baffles with a length of 100 μm (b), separated by interspaces of 100 μm (i). Liposomes were fabricated *via* nanoprecipitation by diluting a lipid-containing ethanolic solution with an aqueous phase (PBS). As ethanol concentration decreases, lipids self-assemble first into discs and subsequently into vesicles.

Analysis of molds by scanning electron microscopy (SEM)

Samples were sputter-coated with a 60/40 gold/palladium layer for 6 min using a SC7620 Mini Sputter Coater (Quorum Technologies, Lewes, UK) to enhance conductivity and prevent charge build-up. SEM imaging was performed using a ZEISS EVO 10 electron microscope (Carl Zeiss Microscopy GmbH, Jena, Germany) at an accelerating voltage of 10 kV and a probe current of 100 pA. Top-view and side-view micrographs were acquired to assess structural integrity, layer thickness, and overall print quality.

Fabrication of microfluidic devices by soft lithography

Polydimethylsiloxane (PDMS, Sylgard 184, Dow Corning, Midland, MI, USA) was thoroughly mixed with its cross-linking agent in a 10:1 ratio using a planetary centrifugal mixer (ARE-250, Thinky Co., Tokyo, Japan). The mixture was then degassed in a desiccator and poured onto the mold. After curing for at least 4 h at 65 °C, replicas were peeled off, and respective inlets and outlets were punched using a biopsy needle with a diameter of 1.2 mm. The replicas were treated with oxygen plasma for 1 min (Atto, Diener electronics GmbH & Co. KG, Ebhausen, Germany) and subsequently bonded to a coverslip.

Preparation and physical characterization of liposomes

1,2-Dioleoyl-*sn-glycero*-3-phosphocholine (DOPC) was kindly provided by Lipoid GmbH (Ludwigshafen, Germany) and dissolved in ethanol at a concentration of 25 mM. The resulting solution and phosphate-buffered saline (PBS, pH 7.4) were filled into syringes, respectively, and connected to the PDMS-based microfluidic device *via* 1/32″ (ID) polytetrafluorethylene (PTFE) tubing. While the flow rate ratio (FRR) was kept constant at 4, the total flow rate (TFR) was varied from 10 to 500 μL min^{-1}. The intensity-weighted hydrodynamic diameter and the polydispersity index (PDI) were routinely measured at 25 °C using dynamic light scattering (DLS) after a prior 1 : 10 dilution in PBS to ensure batch consistency (Zetasizer Ultra, Malvern Panalytical, Malvern, UK).

Visualization of ethanol distribution by confocal fluorescence microscopy (CFM)

For visualization within the channels, the ethanolic solution was supplemented with 200 μg mL^{-1} Rhodamine B (Acros Organics, Geel, Belgium) instead of DOPC. The baffle mixer was placed on the stage of an LSM900 confocal laser scanning microscope (Carl Zeiss, Jena, Germany). Applying a constant FRR of 4 and various TFR, effects on flow dynamics were visualized at the following excitation and emission wavelengths: Ex 561 nm, Em 450 to 700 nm.

Examination of vesicle formation *via* Foerster resonance energy transfer (FRET)

The microfluidic device and the CLSM setup were installed as described above. The ethanolic phase was supplemented with the FRET pair DiO (3,3′-dioctadecyloxacarbocyanine perchlorate, BIOMOL GmbH, Hamburg) and DiI (1,1′-dioctadecyl- 3,3,3′,3′tetramethylindocarbocyanine, Sigma-Aldrich Co., St. Louis, MO, USA) at 100 μM and 200 μM, respectively. When applicable, 25 mM DOPC was further added. Dyes were analyzed individually in the presence of DOPC, as well as in combination with and without the addition of phospholipid under identical flow conditions. Samples were visualized using the following excitation and emission wavelengths: DiO: Ex 488 nm, Em 410–546 nm; DiI: Ex 561 nm, Em 540–700 nm; and the FRET channel (Ex 488 nm, Em 580–700 nm). FRET efficiency was calculated using the corresponding function of the Zeiss ZEN software (Carl Zeiss, Jena, Germany) based on the method of Youvan.[20] Briefly, the ratio of the donor's fluorescence in the presence (F_a) and absence (F) of the acceptor was used to describe the extent of the resulting energy transfer.

$$\text{FRET efficiency} = 1 - \frac{F_a}{F} \quad (1)$$

Confocal Raman microscopy (CRM)

While the same tubing was used as for the already described microfluidic setup, two KDS-210-CE syringe pumps (KD Scientific Inc., Holliston, USA) were applied. A confocal Raman microscope (alpha 300R; Witec GmbH, Ulm, Germany) with a green laser (532 nm, Nd:YAG) at 17.5 mW laser power equipped with a Zeiss N-Achroplan 63×/0.9 water immersion objective (Carl Zeiss Microscopy, LLC, White Plains, NY 10601, USA) was used for all measurements with a lateral resolution of 20 ± 4 μm (see Fig. S4). The integration time was set to 0.5 s. All measurements were performed at 23 ± 2 °C. For each spectrum, cosmic rays were removed, and the background was subtracted using the rolling ball algorithm in Suite SIX (Witec GmbH, Ulm, Germany). Afterwards, the noise was reduced using a low-pass Fourier filter with a cutoff of 0.2, and a mean spectrum was calculated using a running-average filter of size 10, implemented in a custom Python script. If necessary, measurement artifacts were corrected using a mean filter, in which each pixel of the artifact is replaced by the mean of the pixels directly to its left and right. To extract interpretable images, the classical least squares (CLS) method was employed using a customized Python script to differentiate between PDMS, ethanolic, and aqueous phases. Briefly, each spectrum s was approximated as a linear combination of the pure component spectra p by minimizing the residual $\text{error}\left(s - \sum_i c_i p_i\right)$. The resulting coefficients (c_i) were either

Table 1 Raman peak assignment

Peak	Spectral range [cm^{-1}]
CD	2040 to 2300 (ref. 23 and 24)
OD	2320 to 2720 (ref. 25)
CH	2750 to 3100 (ref. 26)
OH	3100 to 3650 (ref. 25 and 27)

visualized directly to delineate the boundaries of PDMS, ethanol, and PBS, or used to calculate ethanol concentrations using a calibration approach analogous to that described in previous studies.[21,22] Peak integrals of specific vibrational bands (Table 1) were used as the basis for quantifying lipid distribution and determining lipid state. Integrals were calculated as the Riemann sum over the corresponding spectral ranges listed in Table 1. To avoid spectral overlap from the solvent and enable Raman-based lipid quantification and characterization, d_6-ethanol (99 atom% D, Carl Roth GmbH + Co. KG, Karlsruhe, Germany) was employed.

Computational fluid dynamics (CFD) simulations

CFD simulations were performed using the simpleFoam solver for turbulent incompressible flows in OpenFoam.[28] Here, a water flow through a two-dimensional channel with the same dimensions as those used in the experiments, but with different flow speeds, was assumed. The simulation was run with 2000-time steps, and a write interval of 5. Turbulence was modeled using Reynolds-averaged simulations with a Newtonian transport model. Channel walls were modeled with a no-slip boundary condition and a zero gradient pressure distribution. The flow lines were calculated using ParaView.[29]

Results

A serpentine micromixer based on the design reported by Kimura *et al.* (Fig. 1, left), featuring 20 rectangular baffles, was employed as a model geometry to investigate the spatially resolved formation of liposomes in microfluidic systems in real time.[19] The baffle structures periodically narrow the channel width from 200 μm to 50 μm, while interspaced regions widen it to 100 μm, creating alternating zones of fluid constriction and expansion. Microfluidic devices were fabricated *via* soft lithography using 3D-printed molds, and the dimensional accuracy of the printlets was confirmed *via* SEM, with deviations below 5% (Fig. S1). Fluid dynamics, liposome formation (Fig. 1, right), and size fluctuations as a function of the TFR were analyzed *via* a combination of CFD, CRM, and CFM.

Influence of TFR on particle size

The relationship between particle size and the applied TFR is the most commonly assessed metric for characterizing microfluidic mixing systems, as increased agitation is usually assumed to enhance mixing efficiency. Consequently, the size and monodispersity of liposomes produced at different TFRs were initially analyzed *via* DLS. Corresponding Reynolds (Re) and Dean (De) numbers, two standard dimensionless parameters for describing flow regimes in microchannels, were calculated as displayed in Fig. S2. Size evaluation revealed a pronounced decrease in the hydrodynamic diameter with increasing TFR (Fig. 2). The steepest decline from a particle size of 116 nm to 83 nm was observed between 50 μL min^{-1} (Re: 10; De: 6) and 100 μL min^{-1} (Re: 20; De: 11), followed by a more gradual, approximately linear reduction up to 300 μL min^{-1} (Re: 61; De: 33). At higher flow rates (400 μL min^{-1} and 500 μL min^{-1}; Re: 82–102; De: 45–56), the particle size plateaued at 45 nm. The PDI varied between samples and could not be directly correlated with the TFR. However, except for the liposomes produced at a TFR of 500 μL min^{-1}, all samples exhibited PDI values below 0.2, indicating adequate monodispersity.

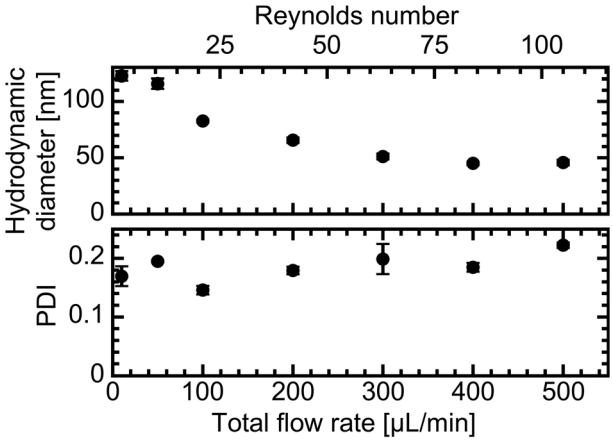

Fig. 2 Influence of the total flow rate (TFR) on liposome size and polydispersity. Liposomes were prepared by diluting an ethanolic solution containing 25 mM DOPC with PBS at a constant flow rate ratio of 4. TFR was varied from 10 μL min^{-1} to 500 μL min^{-1}, and corresponding Reynolds numbers were calculated (see Fig. S2). The hydrodynamic diameter [nm] (top panel) and polydispersity index (PDI, bottom panel) of the resulting liposomes were determined *via* dynamic light scattering (DLS) and are presented as mean values ± standard deviation (n = 3).

Characterization of fluid dynamics and ethanol dilution mechanics

Detailed analyses of the fluid dynamics inside the microchannel were conducted to understand the underlying cause of the observed reduction in vesicle size. Therefore, TFR was systematically varied from 10 μL min^{-1} to 500 μL min^{-1} and dilution of the ethanolic phase was initially visualized for the whole baffle structure by CFM at mid-channel height using rhodamine B as a fluorescent tracer (Fig. S3). As flow differences caused by increasing flow rates were most evident in the first three baffles, these regions were analyzed in greater detail *via in silico* CFD simulations (Fig. 3A). Computation revealed a tortuous flow path as a result of the alternating baffle positioning, with red regions corresponding to high and blue areas to low velocities (Fig. 3B, left). Under conditions characterized by low Reynolds and Dean numbers, such as a Re of 2 and a De of 1 at a TFR of 10 μL min^{-1}, the CFD simulation produced parallel streamlines, confirming a strictly laminar flow regime (Fig. 3B, left). This was in accordance with the CFM micrograph, which revealed distinctly separated ethanol and PBS phases under the same flow conditions (Fig. 3B, right).

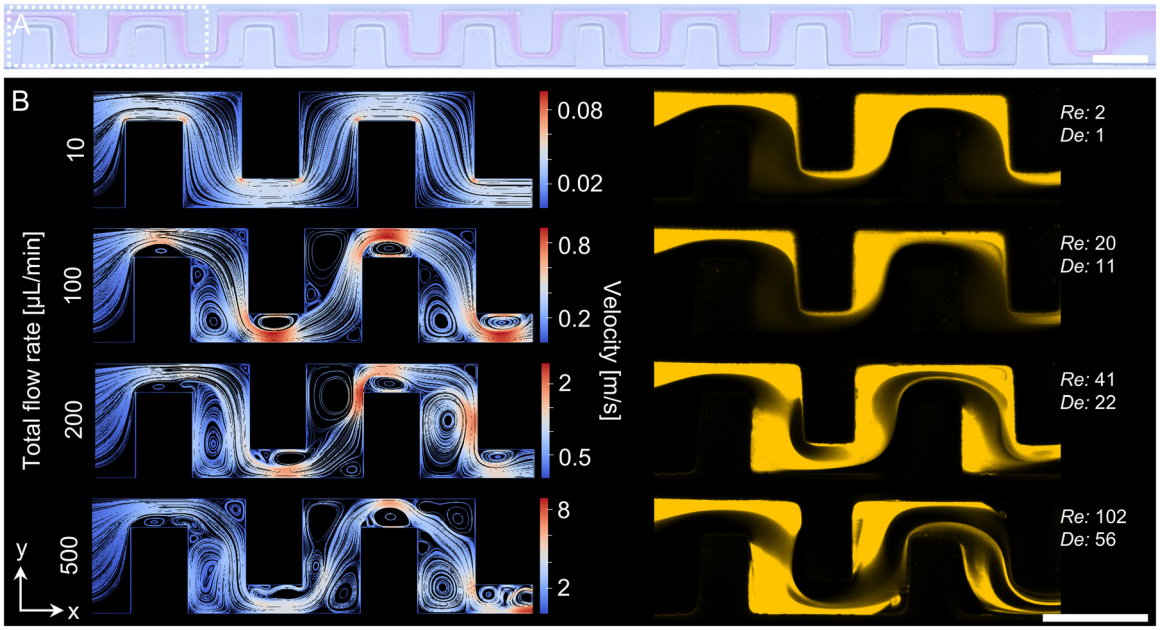

Fig. 3 Influence of total flow rate on fluid flow. A: Brightfield micrograph of the entire channel structure (20 baffles). The ethanolic phase was labeled with rhodamine B for visualization. Images were recorded at a TFR of 10 µL min^{-1} using a 20× magnification (flow direction from left to right). Dotted lines indicate the region selected for computational fluid dynamics (CFD) simulations and in-depth confocal fluorescence microscopy (CFM) analysis. B: Comparison of *in silico* CFD simulations (left) and CFM micrographs (right) within the first four baffles. CFD streamlines represent relative flow velocities, with blue indicating low and red high velocity regions; simulations were performed using water as the working fluid. CFM micrographs show the rhodamine B-labeled ethanolic phase false-colored in yellow (20× magnification). Reynolds numbers (Re) and Dean numbers (De) corresponding to each TFR were calculated. Scale bars represent 200 µm.

Notably, pale halos adjacent to the rhodamine-labeled ethanolic stream may reflect out-of-plane intensity gradients, pointing to three-dimensional flow patterns.

At a TFR of 100 µL min^{-1}, secondary flow structures became apparent in the CFD simulations (Fig. 3B, left). Large vortices developed in low-velocity, low-pressure regions at the baffle corners, while smaller vortices were predicted within the 50 µm-wide constrictions of the baffle structure. These smaller vortices appeared to further compress the flow, resulting in higher local velocities than in other areas of the channel. With increasing flow rate, the number of vortices also expanded, and their distribution shifted from regular to a more heterogeneous pattern along the channel. CFM images at 100 µL min^{-1} showed both phases clearly separated, with no visible indication of secondary flows (Fig. 3B, right). A slight delamination in the upper right corner of the third baffle was observed, which resembled flow dynamics that became more pronounced further downstream of the baffle region (Fig. S3). At 200 µL min^{-1}, distinct alterations in flow patterns were visible in the first baffle: the phases were no longer positioned side by side, and the aqueous phase penetrated the ethanolic phase. At 500 µL min^{-1}, the ethanolic phase additionally formed a vortex in the lower right corner of the second baffle.

At 200 and 500 µL min^{-1}, the phases no longer appeared to be continuous, indicating potential three-dimensional phenomena affecting the flow behavior. To investigate this, multiple cross-sections of selected baffles (I, II, IV, and VIII) were analyzed. Since flow patterns changed prominently when the aqueous phase could break through the ethanolic phase, further analyses were performed at 100 and 500 µL min^{-1} to represent heterogeneous conditions. Cross-sections were visualized using CRM in addition to CFM to exclude potential effects of the fluorescent marker dye on the observed distribution of the ethanolic and aqueous phases (Fig. 4).

Raman spectra were acquired at each scan point of the *x*–*z* cross-sections. To distinguish the channel interior from PDMS, the CLS method was applied, assuming each recorded spectrum to be a linear combination of the pure component spectra of PBS, ethanol, and PDMS (Fig. S4A). The resulting pre-factors represent the quantitative contribution of each compound to the recorded spectrum. Visualization of the PDMS pre-factor enabled a clear differentiation of the channel (blue) from the surrounding PDMS (yellow). Channel boundaries were defined by the contrast between blue and yellow and are indicated by white lines in the subsequent images (Fig. S4B). Ethanol concentrations were calculated by the same method, correlating pre-factors and ethanol concentrations using a premeasured calibration curve. Similar to the CFM-based visualizations of the rhodamine distribution, regions with high ethanol content were rendered in bright yellow. CRM micrographs revealed a progressive decrease in ethanol concentration gradients over the course of the channel. At 100 µL min^{-1}, the cross-section of the first baffle showed that most regions consisted of unmixed solvents, whereas by baffle eight (VIII) the ethanol

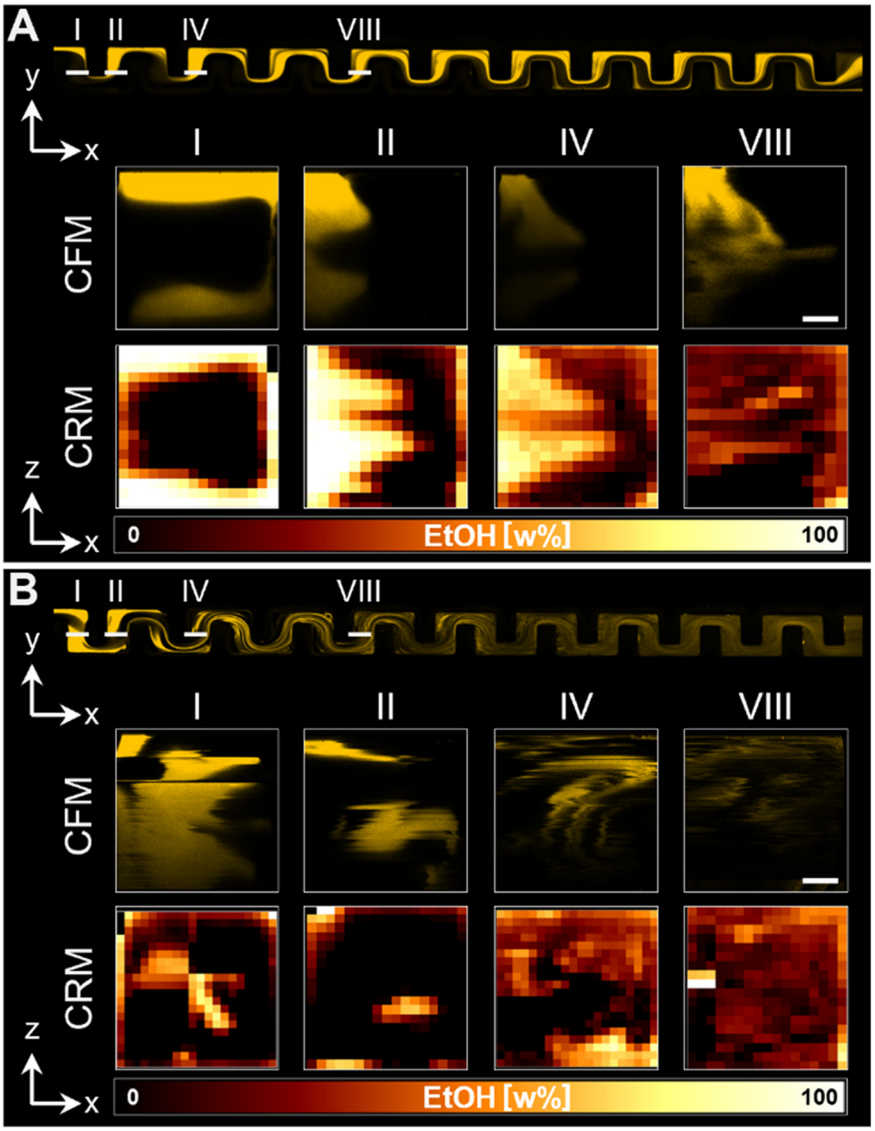

Fig. 4 Spatial distribution of ethanol within the channel *z*-axis *via* confocal fluorescence microscopy (CFM) and Raman microscopy (CRM). Cross-sections through four baffles (I, II, IV, and VIII) were imaged at a TFR of 100 μL min^{-1} (A), and 500 μL min^{-1} (B); their respective position in the baffles are marked in the overview micrographs (top row). For CFM-based measurements, the ethanolic phase was visualized by the addition of rhodamine B (Ex: 561 nm; Em: 450–700 nm); ethanol-rich regions appear yellow. Raman-based ethanol concentration maps were generated using a calibration curve, with yellow indicating areas of high ethanol content and black indicating low concentrations. Scale bars indicate 20 μm.

was already substantially diluted (Fig. 4A). At a TFR of 100 μL min^{-1} the ethanol-rich phase was predominantly located on the right side following odd-numbered baffles and on the left side following even-numbered baffles, as already observed in Fig. 3. At baffle one (I), the ethanolic phase formed a mirrored C-shape, while at baffle two (II) a volcano-like pattern was adopted, which was observed with both methods and reappeared at baffle four (IV). All structures were horizontally symmetric with respect to the channel midline, whereas at baffle eight (VIII), the volcano shape appeared to be less uniform and symmetrical. As expected, based on prior results (Fig. 3), a symmetry break in the cross sections was observed for a TFR of 500 μL min^{-1} (Fig. 4B). However, recorded cross-sections from CFM and CRM still only deviated slightly. While the applied techniques collectively enabled spatially resolved assessment of ethanol dilution within the microfluidic channel, the results alone are insufficient to assess the impact of flow dynamics on liposome formation. Therefore, direct and spatially resolved visualization of liposome formation was pursued at increasing flow rates.

Liposome detection by FRET microscopy

The FRET dye pair of DiO (donor) and DiI (acceptor) was used to visualize particle formation using CLSM. As shown in Fig. 5A, the emission spectrum of DiO overlaps with the excitation spectrum of DiI, enabling energy transfer when both dyes are in close proximity. Given their strong

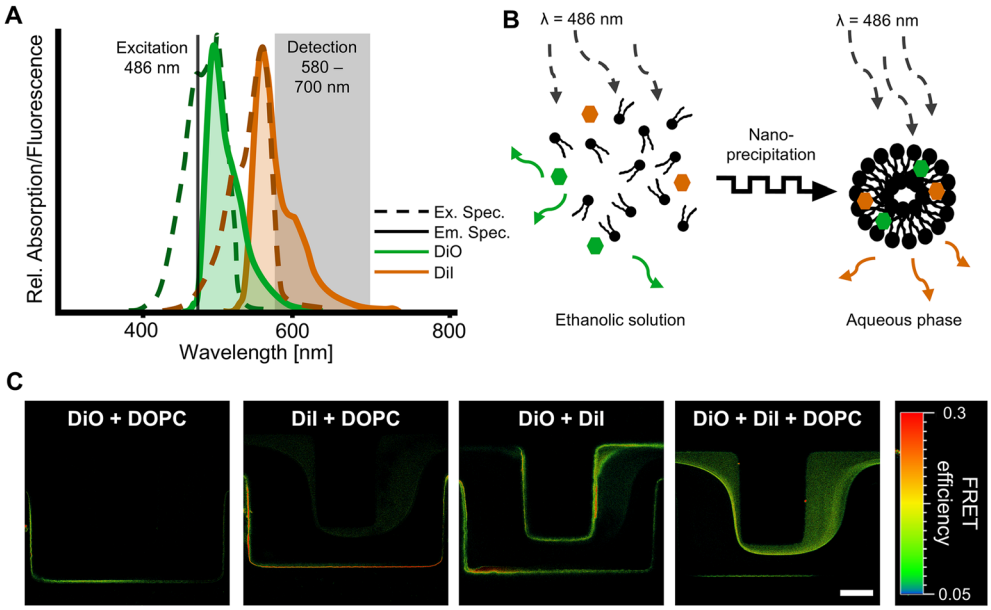

Fig. 5 Principle and application of Foerster resonance energy transfer (FRET) for visualization of liposome formation *via* confocal fluorescence-based microscopy (CFM). A: Excitation (Ex.) and emission (Em.) spectra of DiO (donor) and DiI (acceptor). B: Schematic representation of the FRET mechanism. Upon dilution of the lipid-containing ethanolic phase with aqueous buffer, nanoprecipitation leads to lipid bilayer formation in the microfluidic channel. Due to their hydrophobic nature, both dyes incorporate into the forming lipid bilayer. The resulting proximity between donor and acceptor molecules leads to increased FRET efficiency and increased signal intensity. C: FRET efficiencies calculated from CFM micrographs of the third and fourth baffle (63× magnification). Ethanolic lipid formulations containing different dyes and DOPC combinations were diluted at a TFR of 100 μL min^{-1}. Higher FRET efficiency was only observed when both dyes and lipid were present, indicating successful membrane incorporation. Scale bar represents 50 μm.

hydrophobicity, both dyes are expected to accumulate in lipid bilayers upon their formation, as illustrated in Fig. 5B.[30] Consequently, the efficiency of this energy transfer, typically expressed as FRET efficiency, serves as a proxy for the degree of donor fluorescence quenching by the acceptor. When only one dye and the phospholipid DOPC were pumped through the microfluidic channel at a TFR of 100 μL min^{-1}, calculated FRET efficiencies in the third and fourth baffles remained below the applied lower cut-off threshold of 0.05, which was implemented to minimize signal artifacts from scattering. In contrast, when both dyes but no DOPC were present in the ethanolic phase, increased FRET efficiency was observed near the channel walls. Notably, when all three components, DiO, DiI, and DOPC, were introduced, elevated FRET efficiencies were detected throughout the presumed ethanolic phase, with particularly high values at the interface between the ethanol and PBS streams.

Detection of vesicle formation by CRM

Complementing the FRET experiments, Raman microscopy was employed as a label-free technique to obtain selective, and quantitative information on the physicochemical state of lipids across channel cross-sections. To avoid overlapping of the CH bands from ethanol and lipid signals, deuterated ethanol (d_6-ethanol) was used (Fig. S4A). PDMS and the channel interior were distinguished by the CLS method, as described above (Fig. S4B). The same approach was then used to separate PBS from the lipid-containing d_6-ethanol phase. Visualization of the ratio of PBS to d_6-ethanol pre-factors enabled unambiguous phase identification, with low ratios (yellow) marking the ethanolic phase and high ratios (blue) marking PBS (Fig. 6A). Raman spectra were subsequently acquired within the ethanolic phase, inside the aqueous phase, and at their direct interface (Fig. 6B). As expected, spectra differed strongly in the intensity of the CD and OH peaks, reflecting the respective solvent composition. In addition, apparent alterations in the CH region were observed. The detected CH peak, which is composed of several sub-peaks and shoulders, varied systematically depending on the position within the channel (Fig. 6B). In particular, the distinct bands at approximately 2846 cm^{-1} (CH_a) and 2965 cm^{-1} (CH_b) showed differences in intensity depending on the region analyzed and were used for subsequent quantitative assessment. Calculating the CH_b/CH_a integral ratio, a value of 1.7 was approximated for the ethanolic phase (position a). In contrast, a reduction in the CH_a integral resulted in a slightly higher ratio of 3.2 for the phase interface (position b). Within the PBS phase (position c), the ratio further increased to 7.5. To extend this analysis, the CH_b/CH_a ratio was calculated for each scan point and plotted across the entire *x*–*z*-cross-sections of the indicated baffles (I, IV, and VIII) as shown in Fig. 6.

In situ liposome detection

Due to the lower spatial resolution of CRM, spatially resolved FRET maps were used to assess lipid self-assembly at

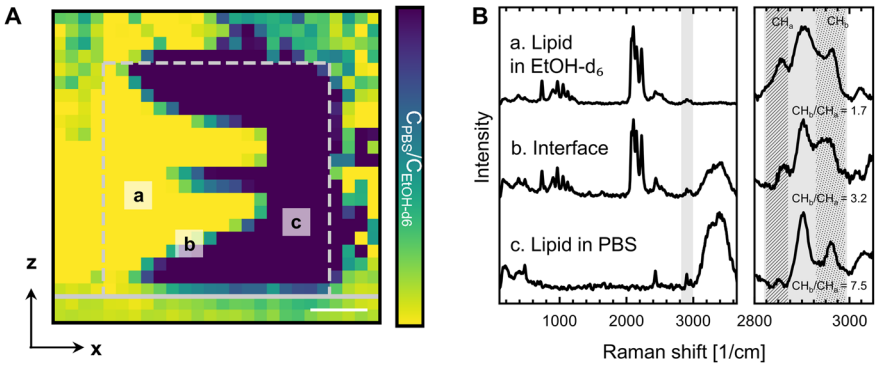

Fig. 6 Analysis of liposome self-assembly process in PDMS microchips using confocal Raman microscopy (CRM). A: Ratio of PBS and EtOH-d_6 CLS factors, distinguishing aqueous and lipid-rich phases in a *x*–*z*-cross-section of the fourth baffle. Raman images were acquired at 5 × 5 μm^2 resolution with a 0.5 s integration time. Scale bar represents 25 μm. B: Raman spectra recorded at three positions (a–c) within the channel (as indicated in panel A). (a) Lipids dissolved in ethanol, (b) the ethanol–aqueous interface, (c) lipid nanocarriers in PBS. All spectra were normalized to their highest peak intensity. The right panel shows normalization to the CH peak. CH_a and CH_b peaks are highlighted, and their integral ratio (CH_b/CH_a) was calculated for each position.

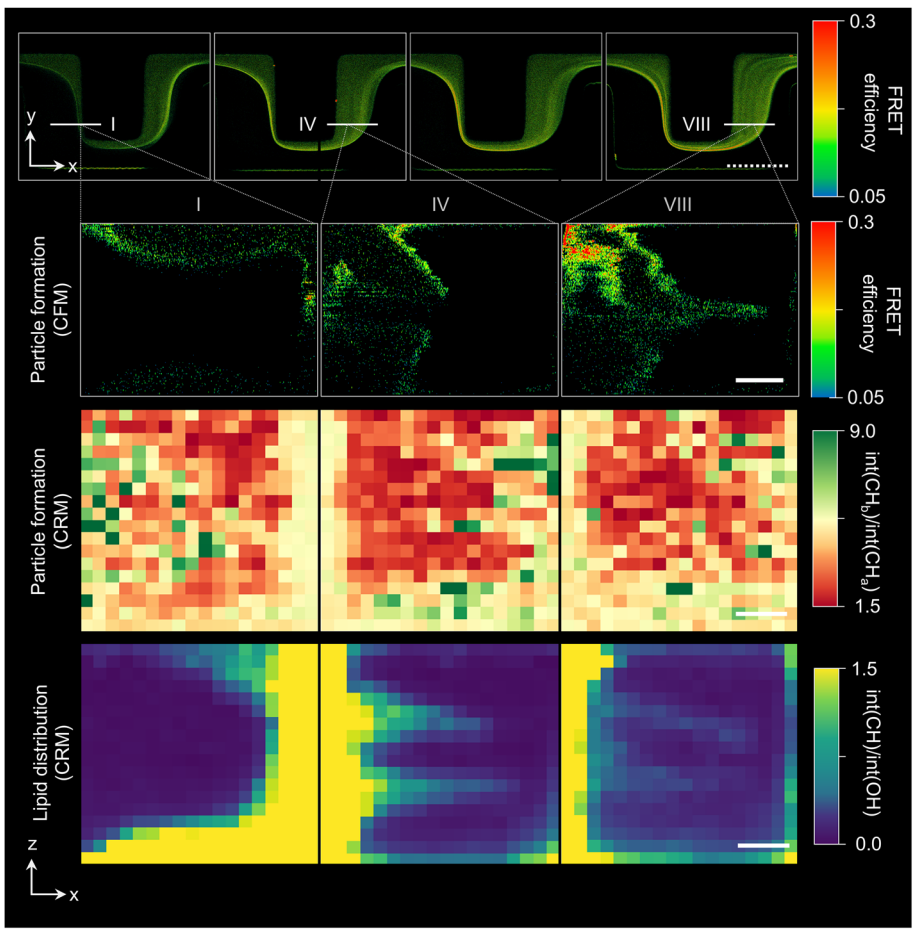

Fig. 7 *In situ* visualization of particle formation in the microfluidic mixing device at a total flow rate of 100 μL min^{-1}. Upper panel: CFM-derived FRET efficiency maps (*x*–*y* cross-sections) across baffles I to VIII (20× magnification). Second to fourth panel: *x*–*z* cross-sections of baffles I, IV, and VIII recorded at 63× magnification. The second panel shows FRET efficiency maps calculated from micrographs obtained *via* CFM. The middle panel illustrates Raman heat maps of CH_b/CH_a peak integrals. The lower panel displays corresponding lipid distribution measured by confocal CRM; yellow indicates high lipid concentrations, and blue indicates low concentrations. Dotted scale bar represents 100 μm; solid scale bar indicates 20 μm.

different positions within the microfluidic device at a TFR of 100 μL min^{-1}. FRET efficiency maps across specific baffles (I to VIII, Fig. 7, upper panel) showed a progressive increase in signal density along the channel. Although most pixel-wise FRET efficiencies remained approximately around 0.1, their spatial distribution became increasingly confined to regions corresponding to the ethanolic phase identified in Fig. 4. The highest efficiencies were consistently located at the center of the channel, matching the interface between the ethanolic and aqueous phases. Similar trends were observed in the *x*–*z* cross-sectional FRET efficiency maps of these baffles (I, IV, and VIII). The number of pixels exceeding a FRET efficiency threshold of 0.05 increased in downstream baffles, while the highest values remained concentrated at the phase interface. Corresponding to prior results (Fig. 4), pixels with elevated FRET efficiencies formed a mirrored C-shape in the first baffle (I) and volcano-like patterns in the later baffles (IV and VIII). A comparable spatial pattern was observed in the CRM datasets by plotting the ratio of the CH_b/CH_a peak integrals. In these images (Fig. 7), values around 3–4 were measured at the interface between the two phases. Lower CH_b/CH_a ratios were observed in regions corresponding to the ethanolic phase, which also showed high lipid abundance. In contrast, higher CH_b/CH_a ratios were detected in PBS-dominated regions, where lipid content was low. This spatial distribution is consistent across multiple cross-sections and follows the same geometric patterns observed in the FRET data.

Discussion

Characterization of flow profiles within microfluidic mixers has traditionally relied on indirect approaches such as CFD simulations or fluorescence-based tracer studies. While such approaches provide essential insights into mixing regimes, they remain limited to two-dimensional projections in most cases. Consequently, they cannot directly offer insight into the spatiotemporal dynamics of solvent dilution and nanocarrier nucleation. This lack of mechanistic resolution complicates the rational design of microfluidic devices, particularly when aiming to maintain product quality in high-throughput approaches required for industrial manufacturing. Despite the great potential of microfluidics for reproducible nanocarrier production, these uncertainties in flow-formulation relationships continue to hinder scale-up efforts.

Integrating complementary three-dimensional analytical techniques, this study aimed to close this gap by establishing an analytical toolset for real-time *in situ* characterization of nanocarrier formation within a static microfluidic mixer. Using confocal fluorescence-based microscopy, which offers a straightforward approach for visualizing solvent mixing within microfluidic channels, provides high spatial and temporal resolution of the baffle structures. However, this visualization technique inherently relies on fluorescent tracer dyes, which may not fully reflect the ethanol distribution and can potentially alter local fluid–fluid interactions.[18] To overcome these limitations and obtain label-free insight, confocal Raman microscopy was implemented. Commonly used in pharmaceutical research, this technique enables direct and label-free quantification of ethanol dilution without the need for markers.[21,22,31–34] As a Raman spectrum is recorded at each scan point, the information density is remarkably high, and different phases can be distinguished based on their unique Raman wavenumbers. Contextualizing this combinatory approach, the self-assembly of lipids into liposomes was first examined by mixing a lipid-containing ethanolic solution with an aqueous (PBS) phase at different TFRs.

Upon dilution, the lipid concentration exceeds its solubility in the ethanol–water mixture, triggering precipitation into bilayer disk intermediates. Driven by their concentration gradient, lipid species are subsequently transported into increasingly aqueous regions along the channel, where progressive solvent exchange promotes further organization of these intermediates and their self-assembly into liposomes, driven by the amphiphilic nature of the lipids. Faster dilution of the ethanolic lipid solution reduces the time available for disk growth before vesicle closure, resulting in smaller liposomes. Consequently, particle size is expected to decrease with increasing mixing efficiency (Fig. 1).[35,36] Consistent with this assumption, increasing the TFR resulted in a reduction of the hydrodynamic diameter of the nanocarriers, whereas no systematic trend was observed for the PDI (Fig. 2). The decrease in particle size at higher TFRs can be explained by more rapid dilution of the ethanolic lipid solution, a mechanism widely described in the context of microfluidic nanoprecipitation.[37–39]

In-depth analyses of two-dimensional flow patterns within the anterior baffles were conducted by combining *in silico* and experimental methods, including CFD simulations and CFM-based tracing of rhodamine B. The dimensionless Reynolds number, shown in Fig. 3 and calculated as described in Fig. S2, is commonly used to characterize fluid flow regimes, as it expresses the ratio of inertial to viscous forces. In the present study, none of the investigated conditions approached the classical critical Reynolds number of approximately 2300 for the onset of turbulence in straight channels. Consequently, the flow can be assumed to remain laminar over the entire range investigated, and turbulent mixing can be excluded. Mixing is therefore primarily governed by diffusion and geometry-induced advection.[40] Nevertheless, the presence of alternating baffles and curved channel segments may induce secondary flow structures as inertial effects correlate with increasing Re. In curved microchannels, centrifugal forces act on the fluid, leading to secondary Dean flows. The onset and strength of these flows are commonly characterized by the Dean number (De), which incorporates both inertial effects and channel curvature.[41–43] At low total flow rates (TFRs), for example 10 μL min^{-1}, corresponding to a De of approximately 1, the flow remained fully laminar throughout the entire baffle structure, and no

indication of secondary flow was observed (Fig. 3 and S2). Although no distinct phase delamination occurred under these conditions, CFM *x*–*y* cross-sections already suggested the emergence of a weak three-dimensional flow profile. Shallow yellow shadows were visible even at the first baffle, indicating slight out-of-plane displacement of the ethanolic phase carrying the fluorescent tracer.

At higher TFRs, these effects became more pronounced. At 100 μL min^{-1} (De = 11), the yellow shadowing persisted, and phase delamination became apparent in the second half of the baffle structure (Fig. S2). Corresponding CFM and CRM *x*–*z* cross-sections corroborated these observations and revealed a stratified phase distribution, with the ethanolic stream displaced toward the channel ceiling and floor, while the aqueous phase remained concentrated near the channel center (Fig. 4). This behavior is consistent with literature reports, which describe the onset of Dean vortices in microchannels at Dean numbers typically between 10 and 20.[41–43]

In the present geometry, the formation of Dean vortices can be attributed to the alternating arrangement of the baffles, which induces a meandering flow path and generates centrifugal forces in combination with pressure gradients in the vertical (*z*) direction. At mid-channel height, the pressure of the aqueous phase toward the outer channel wall reaches a maximum, resulting in the formation of two counter-rotating Dean vortices.[41–43] These vortical structures could be visualized in the CFM data as shadowing beneath the focal plane, as well as in the cross-sectional views, where mirrored C-shaped and volcano-like intensity patterns were observed (Fig. 4).[42–45] Owing to the symmetry of the Dean vortices with respect to the horizontal mid-plane, the resulting flow structures also exhibited a corresponding symmetry.

At higher TFRs (>100 μL min^{-1}), chaotic advection and the emergence of secondary flow structures disrupted the symmetry of the laminar regime and promoted partial phase delamination. The most pronounced decrease in particle size, which was observed at TFRs between 50 μL min^{-1} and 200 μL min^{-1}, matched with the start of these flows, as confirmed by CFM measurements (Fig. 3B). While CFD simulations predicted mainly similar streamline distributions at 100 μL min^{-1} and 200 μL min^{-1}, CFM already revealed substantial changes in ethanol distribution at the first baffle. Consistent with these findings, Kimura *et al.* reported the appearance of secondary flows in a similar baffle geometry at flow rates of approximately 100 μL min^{-1}.[19]

At a TFR of 200 μL min^{-1}, ethanol was increasingly deflected into the low-pressure zone on the left side of the baffle, marking the onset of vertical phase mixing. According to the CFD results, these low-pressure zones arose from additional vortices in the *x*–*y* plane, which increased in number and size with rising flow rates (Fig. 3). Accordingly, with higher flow rates, the flow patterns also appeared to be governed less by Dean vortices and more by pressure-gradient-driven redistribution of ethanol. This trend became even more pronounced at the highest tested TFR of 500 μL min^{-1}. Phase delamination was already evident at the first baffle in the cross-sections shown in Fig. 4B, and by the third baffle, the two streams could no longer be distinguished clearly. In addition, three-dimensional vortices formed at the corners in front of and behind the baffles (Fig. S3). At a TFR of 200 μL min^{-1}, these corner vortices first appeared around the eleventh baffle but emerged as early as the second baffle at 500 μL min^{-1}, reflecting the increased influence of the low-pressure zones observed in the CFD. These pressure gradients boost the convective phase and ethanol dilution, thereby shifting the zones where lipid self-assembly is most likely to occur.[46]

These findings highlight the importance of multimodal, three-dimensional analysis for characterizing flow dynamics in microfluidic systems. While microscopy-based techniques provide cross-sectional insight into phase distribution and mixing behavior, they often lack the resolution to capture the global streamline structure. In contrast, CFD simulations enable efficient, two-dimensional visualization of full-channel flow fields, but may overlook vertical redistribution or subtle out-of-plane effects, and three-dimensional calculations over extended channel segments are data-heavy and often not feasible. As demonstrated in this study, a combination of both approaches is crucial for fully capturing and resolving complex flow phenomena within structured microfluidic mixers. Despite generating valuable insights into the dynamics of ethanol dilution and highlighting regions where nanoprecipitation is most likely to occur, this approach remains indirect and inherently limited in its ability to spatiotemporally visualize nanocarrier assembly.

To overcome this limitation, this study aimed to directly resolve the *in situ* formation of nanocarriers. As no previous work has reported the real-time visualization of such processes within a microfluidic device, a novel analytical toolset was established to monitor nanoprecipitation during flow. Fluorescence- and Raman-based confocal imaging approaches successfully detected signals specific to liposome formation that were absent in control experiments, confirming their suitability for monitoring nanoprecipitation. While monitoring FRET efficiency, which increases upon close lipid-lipid interactions, served as an indicator of vesicle assembly, complementary Raman spectroscopy provided molecularly specific information on lipid vibrational modes, enabling label-free confirmation of lipid enrichment and structural rearrangements (Fig. 7). Across all cross-sections, particle formation was observed predominantly at the aqueous–ethanol interface, which is consistent with precipitation driven by ethanol dilution. This observation aligns with theoretical predictions and previous experimental studies that describe solvent exchange at the interface as the main driver of lipid self-assembly.[37,47] Notably, even at the eighth baffle, where partial phase delamination became apparent, localized particle formation remained detectable. Thus, the complementary use of CFM and CRM proved especially valuable, as both techniques produced consistent and mutually supportive results. They not only allowed

discrimination between solvent dilution dynamics but also nanocarrier nucleation, processes that are often inferred only indirectly. This consistency is particularly striking as CFM and CRM experiments were performed in independent laboratories, using different syringe pumps and PDMS replicas. In addition, the CRM set-up is based on an upright system, CFM-based imaging was conducted using an inverted microscope. Consequently, gravitational effects on fluid flow must be considered, as two phases of varying densities were used in addition to differences in micromixer placement during measurement. Although density gradients could, in principle, lead to phase interface rotation and might account for minor differences between the CRM and CFM micrographs (Fig. 4 and 7), their influence appeared negligible under the applied conditions, supporting the overall reproducibility of the setup.[21]

Taken together, the integration of FRET efficiency and Raman-based measurements into more standardized fluorescent tracer mapping establishes a robust framework for three-dimensional characterization of microfluidic nanoprecipitation. CFM-based analysis of ethanol distribution and particle formation provides high spatial resolution and rapid acquisition, making it particularly suitable for geometry optimization and process development. Entire channel structures can be imaged to identify regions of intensified ethanol dilution and nanocarrier formation, and flow features emerging at higher TFRs may be directly linked to reduced particle size. This opens opportunities for the rational design of micromixers tailored to specific flow-rate regimes and particle-size targets, as well as for more systematic scale-up of microfluidic devices. The applied additive manufacturing approach for PDMS molds not only enables versatile and rapid fabrication of diverse channel geometries but also allows the production of fully 3D-printed microfluidic chips, thereby overcoming the limitations of PDMS in terms of robustness and pressure resistance.[48] Raman microscopy, by contrast, provides label-free analysis and is, thus, well suited for in-process quality control.[49–51] Raman-based measurements could, in principle, be integrated as an analytical tool into industrial frameworks at selected stages of the fabrication workflow to assess process consistency during large-scale production. In particular, monitoring ethanol-related Raman signal intensity could be used to detect fluctuations in solvent composition and mixing efficiency. Extending this concept, the CH_b/CH_a band ratio provides a more chemically specific metric for lipid precipitation events and lipid incorporation into liquid-crystalline bilayers. While such information would be highly valuable for comparing particle formation across different lipid chemistries or formulation compositions during process development and scale-up attempts, its practical implementation in an industrial environment is more challenging. In the present study, deuterated ethanol was employed to avoid spectral overlaps between ethanol and lipid C–H vibrations; under manufacturing-relevant conditions using non-deuterated solvents, more sophisticated and data-heavy analyses would be required to distinguish the respective Raman peaks reliably. However, the developed combinatory toolset helps to address current challenges in applying microfluidic approaches to the scalable fabrication of pharmaceutical products in accordance with regulatory requirements. In particular, gaining a deeper understanding of flow patterns and the fluid-dynamic mechanisms underlying particle formation may accelerate the scale-up of device geometries and enable more precise process design and control.

Conclusions

This study addresses a methodological gap in the characterization of microfluidic mixers by establishing a complementary three-dimensional analytical toolset to directly monitor flow behavior, mixing of fluid phases, and nanocarrier formation *in situ*. Whereas established CFD simulations and CFM-based visualization provided valuable information on ethanol distribution and general fluid behavior, the integration of Raman and FRET microscopy facilitated spatially resolved, real-time imaging of nanocarrier nucleation within the microchannel. The use of different advanced microscopy techniques not only advances mechanistic understanding but also establishes a robust toolset for future process engineering, optimization, and control. While Raman microscopy offers a promising route toward industrial in-process quality control, the developed FRET-based CFM method paves the way for easier rational mixer design and geometry optimization in the future. Together with additive manufacturing technologies, such as three-dimensional printing, can enable highly flexible, geometry-tailored microfluidic platforms, thereby accelerating the industrial large-scale production of nanosized therapeutics.

Author contributions

Christopher Hauss: conceptualization, data curation, formal analysis, investigation, methodology, software, validation, visualization, writing – original draft, writing – review and editing. Alexander Erb: data curation, formal analysis, investigation, methodology, software, visualization, writing – original draft, writing – review and editing. Johannes Most: investigation, visualization. Johanna Steimann: investigation. Robert W. Stark: funding acquisition, resources, writing – review and editing. Stefanie Gier: supervision, visualization, writing – original draft, writing – review and editing. Maike Windbergs: funding acquisition, project administration, resources, writing – original draft, writing – review and editing.

Conflicts of interest

The authors declare no conflict of interest.

Data availability

Recorded Raman data for this article are available from TUDataLib at https://tudatalib.ulb.tu-darmstadt.de/items/a8b32f3a-910c-4f15-ae00-6bc45883b26b. Additional data will be made available upon reasonable request by the corresponding author. Supplementary information (SI) is available. See DOI: https://doi.org/10.1039/d5lc00947b.

Acknowledgements

This study was supported by the Federal Ministry of Education and Research (BMBF, Proxidrugs-BioDEL, grant 03ZU2109GA) and the German Research Foundation (DFG, Deutsche Forschungsgemeinschaft) *via* the SFB 1194 "Interaction between Transport and Wetting Processes", Project ID 265191195, Project A07.

References

1 H.-K. Chan and P. C. L. Kwok, Production methods for nanodrug particles using the bottom-up approach, *Adv. Drug Delivery Rev.*, 2011, **63**, 406–416.
2 B. Sinha, R. H. Müller and J. P. Möschwitzer, Bottom-up approaches for preparing drug nanocrystals: formulations and factors affecting particle size, *Int. J. Pharm.*, 2013, **453**, 126–141.
3 V. Harish, M. M. Ansari, D. Tewari, M. Gaur, A. B. Yadav and M.-L. García-Betancourt, *et al.*, Nanoparticle and nanostructure synthesis and controlled growth methods, *Nanomaterials*, 2022, **12**, 3226.
4 Y. Bi, S. Xie, Z. Li, S. Dong and L. Teng, Precise nanoscale fabrication technologies, the "last mile" of medicinal development, *Acta Pharm. Sin. B*, 2025, **15**, 2372–2401.
5 S. Đorđević, M. M. Gonzalez, I. Conejos-Sánchez, B. Carreira, S. Pozzi and R. C. Acúrcio, *et al.*, Current hurdles to the translation of nanomedicines from bench to the clinic, *Drug Delivery Transl. Res.*, 2022, **12**, 500–525.
6 U.S. Department of Health and Human Services, Food and Drug Administration, Liposome Drug Products: Chemistry, Manufacturing, and Controls; Human Pharmacokinetics and Bioavailability; and Labeling Documentation, Guidance for Industry, April 2018, available from: https://www.fda.gov/media/70837/download.
7 S. Mehraji and D. L. DeVoe, Microfluidic synthesis of lipid-based nanoparticles for drug delivery: recent advances and opportunities, *Lab Chip*, 2024, **24**, 1154–1174.
8 C. Moino, F. Artusio and R. Pisano, Shear stress as a driver of degradation for protein-based therapeutics: more accomplice than culprit, *Int. J. Pharm.*, 2024, **650**, 123679.
9 A. Becskei and S. Rahaman, The life and death of RNA across temperatures, *Comput. Struct. Biotechnol. J.*, 2022, **20**, 4325–4336.
10 M. Mehta, T. A. Bui, X. Yang, Y. Aksoy, E. M. Goldys and W. Deng, Lipid-Based Nanoparticles for Drug/Gene Delivery: An Overview of the Production Techniques and Difficulties Encountered in Their Industrial Development, *ACS Mater. Au*, 2023, **3**, 600–619.
11 F. P. Polack, S. J. Thomas, N. Kitchin, J. Absalon, A. Gurtman and S. Lockhart, *et al.*, Safety and efficacy of the BNT162b2 mRNA Covid-19 vaccine, *N. Engl. J. Med.*, 2020, **383**, 2603–2615.
12 L. R. Baden, H. M. El Sahly, B. Essink, K. Kotloff, S. Frey and R. Novak, *et al.*, Efficacy and safety of the mRNA-1273 SARS-CoV-2 vaccine, *N. Engl. J. Med.*, 2021, **384**, 403–416.
13 H. I. Labouta, R. Langer, P. R. Cullis, O. M. Merkel, M. R. Prausnitz and Y. Gomaa, *et al.*, Role of drug delivery technologies in the success of COVID-19 vaccines: a perspective, *Drug Delivery Transl. Res.*, 2022, **12**, 2581–2588.
14 S. J. Shepherd, D. Issadore and M. J. Mitchell, Microfluidic formulation of nanoparticles for biomedical applications, *Biomaterials*, 2021, **274**, 120826.
15 L. Li, Q. Chen, G. Sui, J. Qian, C.-T. Tsai and X. Cheng, *et al.*, A Three-Dimensional Micromixer Using Oblique Embedded Ridges, *Micromachines*, 2021, **12**, 806.
16 W.-F. Fang, M.-H. Hsu, Y.-T. Chen and J.-T. Yang, Characterization of microfluidic mixing and reaction in microchannels via analysis of cross-sectional patterns, *Biomicrofluidics*, 2011, **5**, 014111.
17 M. Hejazian, E. Balaur and B. Abbey, Recent Advances and Future Perspectives on Microfluidic Mix-and-Jet Sample Delivery Devices, *Micromachines*, 2021, **12**, 531, DOI: 10.3390/mi12050531.
18 C. Diddens, P. J. Dekker and D. Lohse, Non-monotonic surface tension leads to spontaneous symmetry breaking in a binary evaporating drop, *arXiv*, 2024, preprint, arXiv:2402.17452 [physics], DOI: 10.48550/arXiv.2402.17452.
19 N. Kimura, M. Maeki, Y. Sato, Y. Note, A. Ishida and H. Tani, *et al.*, Development of the iLiNP device: fine tuning the lipid nanoparticle size within 10 nm for drug delivery, *ACS Omega*, 2018, **3**, 5044–5051.
20 G. W. Gordon, G. Berry, X. H. Liang, B. Levine and B. Herman, Quantitative fluorescence resonance energy transfer measurements using fluorescence microscopy, *Biophys. J.*, 1998, **74**, 2702–2713.
21 A. Erb, J. Vetter, J. Steinmann, A. Blaeser and R. W. Stark, Interdiffusion in microfluidic interface rotation between two laminarly flowing liquids of different densities, *Phys. Fluids*, 2025, **37**, 033613.
22 A. Erb, J. Kind, T. L. Zankel, R. W. Stark and C. M. Thiele, Visualization and quantification of local concentration gradients in evaporating water/glycerol droplets with micrometer resolution, *Proc. Natl. Acad. Sci. U. S. A.*, 2025, **122**, e2423660122.
23 J. Xu, D. Zhu, A. D. Ibrahim, C. C. R. Allen, C. M. Gibson and P. W. Fowler, *et al.*, Raman deuterium isotope probing reveals microbial metabolism at the single-cell level, *Anal. Chem.*, 2017, **89**, 13305–13312.
24 Y. Song, L. Cui, J. A. S. López, J. Xu, Y.-G. Zhu and I. P. Thompson, *et al.*, Raman-Deuterium Isotope Probing for in-

situ identification of antimicrobial resistant bacteria in Thames River, *Sci. Rep.*, 2017, **7**, 16648.
25 M. B. Hahn, F. Uhlig, T. Solomun, J. Smiatek and H. Sturm, Combined influence of ectoine and salt: spectroscopic and numerical evidence for compensating effects on aqueous solutions, *Phys. Chem. Chem. Phys.*, 2016, **18**, 28398–28402.
26 J. Giancaspro, P. Scollan, J. Rosario, E. Miller, S. Braziel and S. Lee, Structural determination of model phospholipid membranes by Raman spectroscopy: laboratory experiment, *Biochem. Mol. Biol. Educ.*, 2022, **50**, 181–192.
27 Q. Hu, S. Ouyang, J. Li and Z. Cao, Raman spectroscopic investigation on pure D2O/H2O from 303 to 573 K: interpretation and implications for water structure, *J. Raman Spectrosc.*, 2017, **48**, 610–617.
28 H. G. Weller, G. Tabor, H. Jasak and C. Fureby, A tensorial approach to computational continuum mechanics using object-oriented techniques, *Comput. Phys.*, 1998, **12**, 620–631.
29 U. Ayachit, A. Bauer, B. Geveci, P. O'Leary, K. Moreland, N. Fabian and J. Mauldin, *Proc. 1st Workshop on In Situ Infrastructures for Enabling Extreme-Scale Analysis and Visualization*, Austin, TX, USA, 2015, pp. 25–29.
30 S. L. Yefimova, I. Y. Kurilchenko, T. N. Tkacheva, N. S. Kavok, I. N. Todor and N. Y. Lukianova, *et al.*, Microspectroscopic study of liposome-to-cell interaction revealed by Förster resonance energy transfer, *J. Fluoresc.*, 2014, **24**, 403–409.
31 Y. Numata, Y. Iida and H. Tanaka, Quantitative analysis of alcohol–water binary solutions using Raman spectroscopy, *J. Quant. Spectrosc. Radiat. Transfer*, 2011, **112**, 1043–1049.
32 P. Rostami, A. Erb, R. Azizmalayeri, J. Steinmann, R. W. Stark and G. K. Auernhammer, Coalescence of viscoelastic drops on a solid substrate, *Phys. Rev. Fluids*, 2025, **10**, 063603.
33 A. K. Bell, J. Kind, M. Hartmann, B. Kresse, M. V. Höfler and B. B. Straub, *et al.*, Concentration gradients in evaporating binary droplets probed by spatially resolved Raman and NMR spectroscopy, *Proc. Natl. Acad. Sci. U. S. A.*, 2022, **119**, e2111989119.
34 A. R. Flanagan and F. G. Glavin, Open-source Raman spectra of chemical compounds for active pharmaceutical ingredient development, *Sci. Data*, 2025, **12**, 498.
35 D. D. Lasic, The mechanism of vesicle formation, *Biochem. J.*, 1988, **256**, 1–11.
36 D. D. Lasič, A general model of vesicle formation, *J. Theor. Biol.*, 1987, **124**, 35–41.
37 M. Maeki, Y. Fujishima, Y. Sato, T. Yasui, N. Kaji and A. Ishida, *et al.*, Understanding the formation mechanism of lipid nanoparticles in microfluidic devices with chaotic micromixers, *PLoS One*, 2017, **12**, e0187962.
38 G.-S. Na, J.-U. Joo, J. Y. Lee, Y. Yun, B. K. Kaang and J.-S. Yang, *et al.*, Full-cycle study on developing a novel structured micromixer and evaluating the nanoparticle products as mRNA delivery carriers, *J. Controlled Release*, 2024, **373**, 161–171.
39 J. Y. Han, J. N. La Fiandra and D. L. DeVoe, Microfluidic vortex focusing for high throughput synthesis of size-tunable liposomes, *Nat. Commun.*, 2022, **13**, 6997.
40 C. K. Chung, C. Y. Wu and T. R. Shih, Effect of baffle height and Reynolds number on fluid mixing, *Microsyst. Technol.*, 2008, **14**, 1317–1323.
41 R.-T. Tsai and C.-Y. Wu, An efficient micromixer based on multidirectional vortices due to baffles and channel curvature, *Biomicrofluidics*, 2011, **5**, 014103.
42 N. Nivedita, P. Ligrani and I. Papautsky, Dean flow dynamics in low-aspect ratio spiral microchannels, *Sci. Rep.*, 2017, **7**, 44072.
43 Y. C. Wong, C. Dai, Q. Xian, Z. Yan, Z. Zhang and W. Wen, Flow study of Dean's instability in high aspect ratio microchannels, *Sci. Rep.*, 2023, **13**, 17896.
44 M. G. Lee, S. Choi and J.-K. Park, Rapid laminating mixer using a contraction-expansion array microchannel, *Appl. Phys. Lett.*, 2009, **95**, 051902, DOI: 10.1063/1.3194137.
45 V. S. Sivasankar, Y. Wang, R. Natu, D. Porter, L. Herbertson and B. A. Craven, *et al.*, Particle–liquid transport in curved microchannels: effect of particle volume fraction and size in Dean flow, *Phys. Fluids*, 2022, **34**, 053304.
46 M. Yu, D. Liu, P. Shah, B. Qiu, A. Mathew, L. Yao, T. Guan, H. Cong and N. Zhang, Optimizing microfluidic channel design with tilted rectangular baffles for enhanced mRNA-lipid nanoparticle preparation, *ACS Biomater. Sci. Eng.*, 2025, **11**, 3762–3772, DOI: 10.1021/acsbiomaterials.4c02373.
47 M. Maeki, T. Saito, Y. Sato, T. Yasui, N. Kaji, A. Ishida, H. Tani, Y. Baba and H. Harashima, A strategy for synthesis of lipid nanoparticles using microfluidic devices with a mixer structure, *RSC Adv.*, 2015, **5**, 46181.
48 S. Waheed, J. M. Cabot, N. P. Macdonald, T. Lewis, R. M. Guijt, B. Paull and M. C. Breadmore, 3D printed microfluidic devices: enablers and barriers, *Lab Chip*, 2016, **16**, 1993–2013, DOI: 10.1039/C6LC00284F.
49 D. E. Desa, T. Qian and M. C. Skala, Label-free optical imaging and sensing for quality control of stem cell manufacturing, *Curr. Opin. Biomed. Eng.*, 2023, **25**, 100435, DOI: 10.1016/j.cobme.2022.100435.
50 D. H. Müller, M. Börger, J. Thien and H. J. Koß, Bioprocess in-line monitoring and control using Raman spectroscopy and Indirect Hard Modeling (IHM), *Biotechnol. Bioeng.*, 2024, **121**, 2225–2233, DOI: 10.1002/bit.28724.
51 T. De Beer, A. Burggraeve, M. Fonteyne, L. Saerens, J. P. Remon and C. Vervaet, Near infrared and Raman spectroscopy for the in-process monitoring of pharmaceutical production processes, *Int. J. Pharm.*, 2011, **417**, 32–47, DOI: 10.1016/j.ijpharm.2010.12.012.